Materials Today Bio 16 (2022) 100361

Contents lists available at ScienceDirect

Materials Today Bio

journal homepage: www.journals.elsevier.com/materials-today-bio

3D-printed high-density polyethylene scaffolds with bioactive and antibacterial layer-by-layer modification for auricle reconstruction

Junfeiyang Yin [a,1], Jing Zhong [a,e,1], Jiejie Wang [a], Yilin Wang [a], Ting Li [a], Ling Wang [c], Yang Yang [a], Zhifang Zhen [b], Yanbing Li [a], Hongwu Zhang [a], Shizhen Zhong [a,d,***], Yaobin Wu [a,**], Wenhua Huang [a,b,d,*]

[a] Guangdong Engineering Research Center for Translation of Medical 3D Printing Application, Guangdong Provincial Key Laboratory of Medical Biomechanics, National Key Discipline of Human Anatomy, School of Basic Medical Sciences, Southern Medical University, Guangzhou, 510515, China
[b] Guangdong Medical Innovation Platform for Translation of 3D Printing Application, The Third Affiliated Hospital of Southern Medical University, Guangzhou, 510000, China
[c] Biomaterials Research Center, School of Biomedical Engineering, Southern Medical University, Guangzhou, 510515, China
[d] The Affiliated Traditional Chinese Medicine Hospital of Southwest Medical University, Luzhou, 030699, China
[e] Dermatology Hospital, Southern Medical University, Guangzhou, 510091, China

ARTICLE INFO

Keywords:
3D-printed high-density polyethylene
Layer-by-layer approach
Bioactive coating
Antibacterial coating
Auricle reconstruction

ABSTRACT

High-density polyethylene (HDPE) is a promising material for the development of scaffold implants for auricle reconstruction. However, preparing a personalized HDPE auricle implant with favorable bioactive and antibacterial functions to promote skin tissue ingrowth is challenging. Herein, we present 3D-printed HDPE auricle scaffolds with satisfactory pore size and connectivity. The layer-by-layer (LBL) approach was applied to achieve the improved bioactive and antibacterial properties of these 3D printed scaffolds. The HDPE auricle scaffolds were fabricated using an extrusion 3D printing approach, and the individualized macrostructure and porous microstructure were both adjusted by the 3D printing parameters. The polydopamine (pDA) coating method was used to construct a multilayer ε-polylysine (EPL) and fibrin (FIB) modification on the surface of the 3D HDPE scaffold *via* the LBL self-assembly approach, which provides the bioactive and antibacterial properties. The results of the *in vivo* experiments using an animal model showed that LBL-coated HDPE auricular scaffolds were able to significantly enhance skin tissue ingrowth and ameliorate the inflammatory response caused by local stress. The results of this study suggest that the combination of the 3D printing technique and surface modification provides a promising strategy for developing personalized implants with biofunctional coatings, which show great potential as a scaffold implant for auricle reconstruction applications.

1. Introduction

Microtia is a congenital malformation of the external ear, with a prevalence of 0.83–17.4 per 10,000 live births, especially in Asia (3.06 per 10,000 births) [1,2]. Non-absorbable materials and autologous rib cartilage are usually used in cosmetic procedures for treating microtia [3–5]. Among them, porous high-density polyethylene (HDPE, Medpor®) is a promising material for auricle reconstruction because of its biocompatibility, non-degradability, non-toxicity, and its behavior over the lifetime of patients [6,7]. Although Medpor® implants provide great benefits, they may be associated with postoperative complications, such as inflammation, infection, dislocation, and extrusion, because of their physical and chemical properties, such as rigidity, hydrophobicity, and biological inertness [8–11]. In addition, these implants have to be modified through sculpting, molding, and trimming by the surgeon to ensure a suitable fit because of their lack of patient specificity [12]. However, the complex anatomical structure of the auricle is challenging to replicate by hand [13].

* Corresponding author. Southern Medical University, Guangzhou, 510515, China.
** Corresponding author. Southern Medical University, Guangzhou, 510515, China.
*** Corresponding author. Southern Medical University, Guangzhou, 510515, China.
E-mail addresses: Zhszhnfso@126.com (S. Zhong), wuyaobin2018@smu.edu.cn (Y. Wu), hwh@smu.edu.cn (W. Huang).
[1] These authors contributed equally to this work.

https://doi.org/10.1016/j.mtbio.2022.100361
Received 9 May 2022; Received in revised form 4 July 2022; Accepted 9 July 2022
Available online 15 July 2022

Recently, three-dimensional (3D) printing technology has become one of the most efficient and low-cost strategies for creating personalized medical implants, such as 3D printed HDPE scaffolds [14–17]. Implants manufactured using this technology provide the exact dimensions of the patient's anatomical structure, as well as multi-scale microstructures and controllable mechanical properties [18,19]. Unfortunately, most of the present 3D-printed HDPE implants are biologically inert and lack bioactive properties, causing integration problems between the HDPE implant and the host tissues [20–22]. Consequently, developing a bioactive HDPE auricle scaffold remains problematic using only 3D printing.

Surface modification is a promising strategy to modify bioactive functionalization. Recently, polydopamine (pDA) coating has been given more attention as a surface modification because of its excellent adhesion ability [23–25]. Previous research demonstrated that the mussel-inspired pDA coating of a biodegrading elastomeric compound consisting of poly (glycerol sebacate) and polycaprolactone scaffold surface effectively enhanced proliferation, recruitment, and osteogenic differentiation of bone marrow mesenchymal stem cells for craniofacial bone reconstructing [26]. Therefore, we propose that coating with pDA is an effective strategy to enhance the surface bioactivity of HDPE and induce superior tissue ingrowth. However, because the bioactivity and antibacterial abilities of pDA are limited, previous studies have further introduced active groups and antibiotics [27,28]. For example, it has been demonstrated that using mussel-inspired pDA to coat polyetheretherketone surfaces, along with Cu^{2+} and Mn^{2+}, effectively inhibited bacterial proliferation and promoted osteoinduction [29]. To this end, various pDA functional groups are used in this study to modify the surface further and promote surface activity and antibacterial functions of HDPE.

ε-Polylysine (EPL) is a small cationic peptide that can damage cell membranes and eventually lead to bacterial cell death [30–33]. It has broad-spectrum antibacterial effects and is approved by the United States Food and Drug Administration [34]. In addition, unlike antibiotics, such as silver nanoparticles (AgNPs) and quaternary ammonium compounds (QACs), EPL has specific antibacterial properties and shows excellent biocompatibility with negligible cytotoxicity [35–38]. Therefore, EPL was used for further surface modification in this study to enhance surface antibacterial properties. However, since the ability of pDA and EPL to promote tissue vascularization and skin tissue ingrowth were

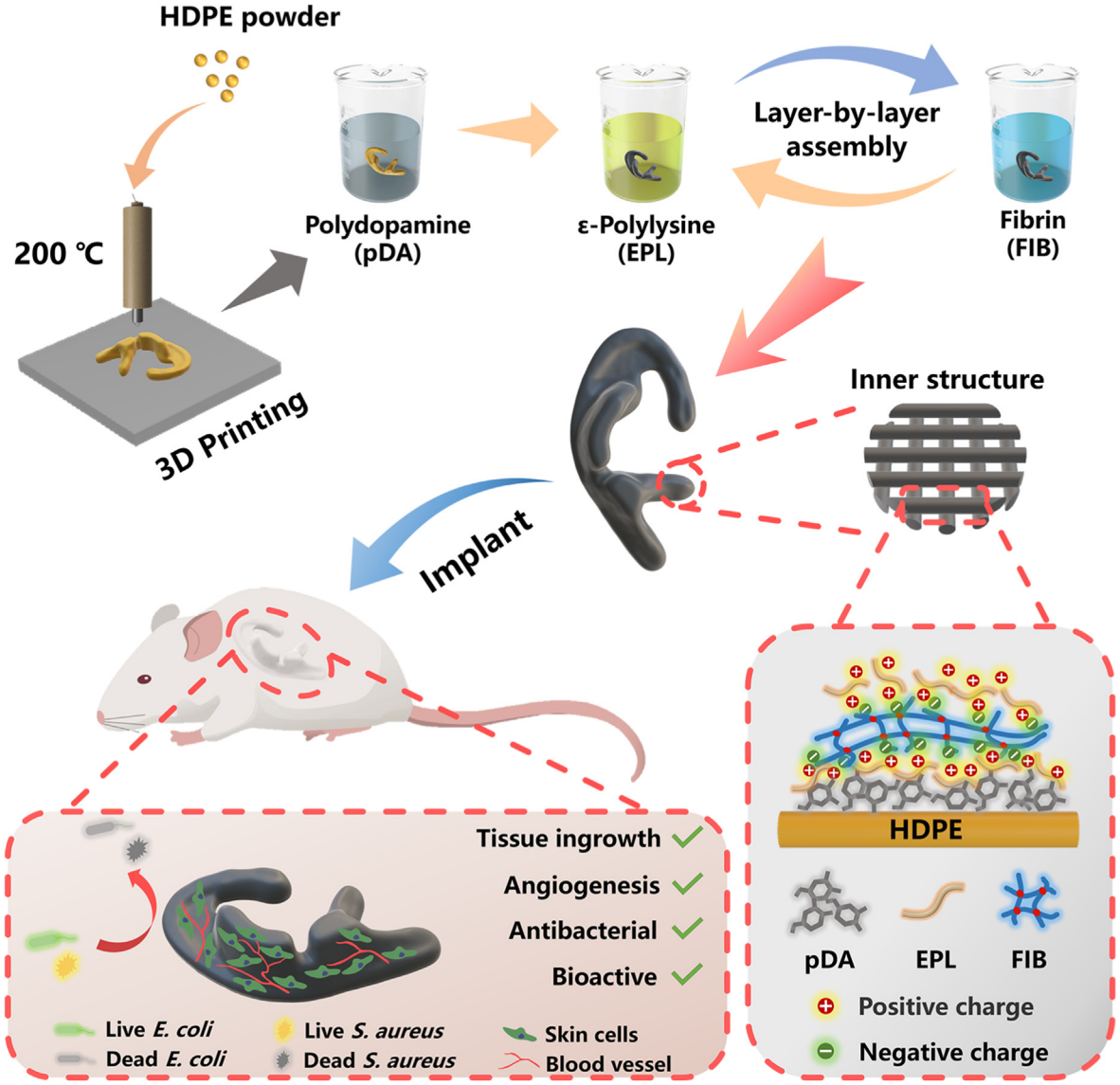

Fig. 1. Schematic illustration of the preparation of the multifunctional pDA-EFE auricle scaffold. The porous HDPE auricle scaffold was first prepared by 3D printing technology. The scaffold was subsequently activated by pDA and coated layer-by-layer with EPL and FIB. The obtained pDA-EFE auricle scaffold had bioactive, antibacterial, angiogenesis enhancing, and tissue ingrowth promoting properties.

insignificant, other bioactive coatings were introduced.

Layer-by-layer (LBL) assembly is a promising approach for fabricating thin multilayer coatings *via* the electrostatic mutual attraction of oppositely charged polyelectrolytes [39,40]. A previous study investigated the conjugation of EPL and pDA to immobilize EPL and gum arabic on titanium using LBL assembly technology. However, gum arabic only acts as an intermediate adhesive and lacks bioactivity [32]. Moreover, fibrin (FIB) plays an essential role in vascular and endothelial tissue regeneration, binds to other cell types and cell adhesion-mediating ECM proteins, and carries a negative charge in the body fluid environment [41–43]. Therefore, we hypothesized that a pDA coating could provide the functional groups that give the HDPE surface hydrophilicity and bioactivity, which can then react with the amino groups in EPL. The effect of pDA coating is then combined with the electrostatic adsorption of FIB to form synergistic LBL assembly functional coatings. Therefore, we propose that applying these coatings on 3D auricle HDPE scaffolds will promote skin tissue integration.

In this study, we developed a 3D printed HDPE auricle scaffold with bioactive and antibacterial modifications to prevent postoperative complications, such as infection, inflammation, and ulceration (Fig. 1). *In vitro* studies confirmed that the LBL coating effectively promotes biocompatibility toward fibroblast cells and inhibits bacteria proliferation. Furthermore, these auricular HDPE scaffolds with LBL coatings were implanted *in vivo* to verify that the HDPE scaffolds promote tissue ingrowth. These data suggest that the LBL-coated 3D auricle HDPE scaffold can alleviate complications commonly seen after conventional auricle reconstruction surgery and promote its integration with skin tissue.

2. Material and methods

2.1. Materials

HDPE powder (Mw = 100, 000) was purchased from Shanghai Youngling Electromechanical Technology Co., Ltd. (Shanghai, China) and dopamine hydrochloride (pDA) from Sigma-Aldrich (USA). ϵ-Polylysine (EPL) was obtained from Macklin (Shanghai, China). Fibrinogen (Fbg) and thrombin were purchased from Acmec (Shanghai, China). Dulbecco's Modified Eagle Medium (DMEM), Dulbecco's phosphate-buffered saline (DPBS), fetal bovine serum (FBS), and streptomycin–penicillin were purchased from Gibco (USA).

2.2. Preparation of pDA-EFE scaffolds

The HDPE scaffolds were fabricated using a 3D bioprinter (Envision TEC, 3D-Bioplotter Developer Series) (Movie S1). Briefly, a series of designed models of dense 2D HDPE and porous 3D HDPE scaffolds were exported to the standard triangulation language files (STL format), which were imported into the Bioplotter RP software for slicing and subsequently loaded into the 3D bioprinter. The following parameters were used for printing the scaffolds: the printing temperature was 200 °C; the nitrogen pressure was 6.5, 7.0, 7.5, or 8 bar; the printing head feed rate was 2, 3, 4, or 5 mm/s; the diameter of the needle used was 300 μm; the distance between strains (Δx) was 300 or 600 μm; and the heating plate temperature was 80 °C. The porous 3D HDPE scaffolds (Φ10 × 0.6 mm, Δx = 600 μm) were used for morphology observation, cell experiments, antibacterial experiments, and implantation experiments.

Supplementary video related to this article can be found at https://doi.org/10.1016/j.mtbio.2022.100361

To enhance surface activity, the HDPE scaffolds were treated with a plasma cleaner (PDC-MG, Chengdu Mingheng Science & Technology, China) at an RF power of 150 W and frequency of 13.56 MHz for 2 min. For the preparation of pDA-coated HDPE scaffolds, the scaffolds were immersed in a 2-mg/mL DA solution (10 mM Tris-HCl, PH = 8.5) and mixed in a shaker at 150 rpm for 12 h at room temperature. The obtained scaffolds were rinsed with deionized water three times and dried at 40 °C for 2 h. Subsequently, the pDA (HDPE-pDA) scaffolds were immersed in 10 mg/mL EPL solution at 37 °C for 12 h. Then, 5 mg/mL of Fbg in 0.9% NaCl solution was adsorbed onto the surface of the pDA-E (HDPE-pDA-EPL) scaffolds at 37 °C for 2 h, followed by rinsing of the scaffolds with 0.9% NaCl solution and activated with thrombin (2.5 U/mL in 1 mM $CaCl_2$ solution) at 37 °C for 30 min. Finally, the pDA-EFE (HDPE-pDA-EPL-FIB-EPL) scaffolds were generated by coating the pDA-EF (HDPE-pDA-EPL-FIB) scaffolds with 10 mg/mL EPL solution at 37 °C for 12 h.

2.3. Characterization of pDA-EFE scaffolds

All scaffolds were dried at 40 °C for 2 h and observed under a microscope (BX 53, Olympus, Japan), making it possible to quickly screen the scaffolds and determine optimal printing parameters. Next, morphological observations of the scaffolds were conducted using a scanning electron microscope (SEM, S–3000 N, Hitachi, Japan) after sputtering with gold at an accelerating voltage of 20 kV. The SEM facility was also equipped with an energy-dispersive spectrometer (EDS) for chemical microanalysis. Additionally, to explore the stability of the pDA coating and the LBL-modified coating, all the prepared scaffolds were immersed in 2 mL DMEM at 37 °C and were observed by the SEM at preset time. The chemical compositions of the samples were further examined using X-ray photoelectron spectroscopy (XPS, K-Alpha+, Thermo, UK). The 2D plain film scaffolds (Φ10 × 0.3 mm, Δx = 300 μm) were used for hydrophilicity testing. The surface zeta potential of the scaffolds was measured in a 10^{-3} KCl solution at PH 7.4, using a zeta potential tester for solid material surfaces (SurPASS 3, Anton Paar, Austria). The water contact angle (WCA) was assessed using the sessile drop method on a droplet analysis system (Theta Flex, Biolin Scientific, Sweden). Briefly, 4 μL of deionized water was dropped on the surface of the sample at room temperature and humidity, and images were taken with a camera after stabilization. The porous 3D porous (Φ5 × 5 mm, Δx = 600 μm) were used for mechanical testing (Fig. S3). The mechanical properties of the scaffolds were tested using a static compression load cell of 500 N at a speed of 2 mm/min using a universal mechanical testing machine (LS1, Ametek, USA). The recorded test data were analyzed to determine the compressive strength and modulus.

2.4. In vitro cytocompatibility and morphological evaluation of L929 cells on pDA-EFE scaffolds

Mouse fibroblast L929 cells were isolated and incubated in DMEM containing 10% FBS, 1% streptomycin–penicillin, and cultured at 37 °C in an environment containing 5% CO_2. The medium was changed every other day until cells were confluent, and the cells were then detached using trypsin-EDTA (Gibco). After sterilization with 75% ethanol for 30 min the cells were seeded in 24-well cell culture plates at a density of 1×10^4 cells/scaffold. On days 1, 3, and 5 after the start of culture, cell proliferation was assessed using the alamarBlue reagent (Invitrogen, USA). Subsequently, 100 μL of each sample solution was transferred to a 96-well plate and read at a wavelength of 530/590 nm using a multifunctional cell imaging microplate detector (Cytation5, BioTek, USA). Fluorescence microscopy (IX 83, Olympus, Japan) observations using a live/dead viability kit (Invitrogen, USA), which stained living cells green and dead cells red were used to assess cell viability.

After culturing the L929 cells on scaffolds for 3 days, they were rinsed with DPBS to remove unattached cells, fixed with 4% paraformaldehyde, stained with phalloidin-FITC (Sigma), and counterstained with DAPI. A confocal laser scanning microscopy (CLSM; LSM800, Zeiss, Germany) was used for imaging. Meanwhile, the L929 cell-laden scaffolds were fixed with 2.5% glutaraldehyde, dehydrated with ethanol at concentrations of 50%, 75%, 95%, and 100% and observed under an SEM to examine the growth and morphology of the cells. The aspect ratio of the cells was measured using the ImageJ software [44].

2.5. In vitro antibacterial property evaluation of E. coli and S. aureus on pDA-EFE scaffolds

All scaffolds were sterilized by soaking in 75% ethanol for 30 min and rinsed with 0.85% NaCl solution three times. The antibacterial properties of the scaffolds were assessed using a live/dead bacterial viability kit (Invitrogen, USA) for staining and SEM, while *S. aureus* (ATCC 25923) and *E. coli* (ATCC 112299) were selected as models. The scaffolds were placed in 24-well culture plates and incubated in 1 mL of bacterial suspension ($\sim 1 \times 10^6$ CFU/mL in LB culture medium) for 4 h at 37 °C. Subsequently, the scaffolds were removed, rinsed with 0.85% NaCl solution three times, and stained with the SYTO-9 and PI dye. A fluorescence microscope (IX 83; Olympus, Japan) was used to observe the stained scaffolds. Finally, the scaffolds adhered to *S. aureus* scaffolds were fixed with 2.5% glutaraldehyde, dehydrated with ethanol at concentrations of 50%, 75%, 95%, and 100%, and observed using SEM. Finally, the fluorescence intensities and bacterial densities of *S. aureus* on different scaffold samples were calculated using the ImageJ software.

2.6. Subcutaneous implantation of pDA-EFE scaffolds in rat

Animal experiments were performed in accordance with the Guidelines for the Care and Use of Laboratory Animals formulated by the Animal Research Committee of Southern Medical University. Fifteen scaffolds were randomly divided into five groups: control group without any HDPE scaffold treatment (n = 3), pDA group (n = 3), pDA-EFE group (n = 3), pDA-S (HDPE-pDA-*S. aureus*) group (n = 3), and pDA-EFE-S (HDPE-pDA-EPL-FIB-EPL-*S. aureus*) group (n = 3). All scaffolds were sterilized in 75% ethanol for 30 min and rinsed with 0.9% NaCl solution three times. Then, pDA-S and pDA-EFE-S scaffolds were further adhered to bacteria by immersing pDA and pDA-EFE scaffolds into an *S. aureus* suspension ($\approx 1 \times 10^8$ CFU/mL) for 5 min at 37 °C. Before implantation, female Sprague-Dawley (SD) rats weighing 160–180 g were anesthetized by injecting an appropriate dose of pentobarbital into the abdominal cavity. Scaffolds were subcutaneously implanted between the skin and fascia into the backs of the rats. On days 7 and 14 after implantation, skin biopsies, including the scaffolds, were harvested for histological analysis. Tissues were fixed, dehydrated, embedded in paraffin, sectioned, and stained with hematoxylin and eosin (H&E), CD68 (Servicebio, China), and DAPI to evaluate their histocompatibility and antibacterial activity.

2.7. Preparation and morphological analysis of auricle-shaped scaffolds

A laser scanner collected the 3D auricle-shaped original data from the Medpor® (Stryker, USA) base framework (Handscan700, Creaform, Canada). The data were imported into Geomagic software (3D Systems, USA) and Touch X Haptic (3D Systems, Rock Hill, SC) to obtain the auricle-shaped model. The model was then scaled to half-size and cut with a coronal plane suitable for implantation in SD rats. As previously described, auricle-shaped HDPE scaffolds (HDPE (auricle)) were manufactured using a 3D bioprinter and coated with pDA, EPL, and FIB. The treated scaffolds were subsequently referred to as pDA-EFE (auricle) (Fig. 8a, Movie S2).

Supplementary video related to this article can be found at https://doi.org/10.1016/j.mtbio.2022.100361

The surface image data were collected from the auricle-shaped scaffold using a laser scanner. These data were further processed using the Geomagic software. The resulting data obtained from the auricle-shaped scaffold were compared with those of the original model. The finite element deviation analysis of the original model was simulated using OptiStruct software (HyperWorks 14.0, Altair, USA) following a previously described method [45]. The model was assigned a density of 0.94 g/cm^3 and Young's modulus of 100 MPa. The boundary condition of the bottom of the model was fixed, and a loading pressure of 0.01 MPa was applied to the auricle-shaped scaffold [46].

2.8. Subcutaneous implantation of auricle-shaped scaffolds in rats

Similar to previous animal experiments, SD rats (n = 6) were divided into two groups, which were used for the *in vivo* compatibility study of auricle-shaped scaffolds. HDPE (auricle) and pDA-EFE (auricle) were subcutaneously implanted between the skin and fascia on the backs of the rats. After 28 days, skin biopsies, including the scaffolds, were divided into two parts for histological and immunohistochemical analyses. Tissues were fixed, dehydrated, embedded in paraffin, sectioned, and stained with H&E, CD68, Sirius red, CD31(Servicebio, China), α-SMA (Servicebio, China), and DAPI to evaluate histocompatibility and vascularization.

2.9. Statistical analysis

The experimental data were assessed using SPSS software and ImageJ software. One-way analysis of variance (ANOVA) was used for all statistical analyses. $P < 0.05$ was considered statistically significant. Statistical charts were drawn using Origin software.

3. Results and discussion

3.1. Fabrication and characterization of pDA-EFE scaffolds

The 3D HDPE scaffold was prepared using extrusion printing, and its structural properties, such as the diameter of the printed filament and the gap of the filaments, were adjusted by determining the optimal printing parameters, including the moving speed and printing pressure (Fig. 2a). In this study, the speed rates ranged from 2 to 5 mm/s and the printing pressures from 6.5 to 8 bar, respectively. As shown in Fig. 2b, the diameters of the printed filaments significantly decreased from 569 ± 2 to 246 ± 4 μm as the speed rate increased from 2 to 5 mm/s when the printing pressure was set to 7.5 bar. In addition, the higher printing pressure also led to a large diameter of filaments but a lower gap distance between filaments. To maintain an optimum porous structure and connectivity for tissue ingrowth and gas-liquid metabolism, the pore size of HDPE was set to approximately 300 μm, which is beneficial for skin tissue ingrowth and scaffold stability *in vivo* [47,48]. Therefore, the optimal printing speed rate and pressure were determined as 4 mm/s and 7.5 bar, respectively, which resulted in a constant extrusion HDPE filament with a diameter of 318 ± 7 μm and a suitable gap distance of 300 μm. It is generally accepted that, for a porous implant, the micropore size of the porous scaffold should be close to 300 μm for better ingrowth of vessels and soft tissue [17]. Therefore, the scaffolds prepared in this study were able to support skin tissue integration.

Moreover, it is necessary to further improve the inert surface of HDPE scaffolds to obtain better multifunctional bioactive coatings. As mentioned above, the pDA coating can generate a stable layer on the substrates, providing a platform for further LBL modification with bioactive factors. After immersion in the DA solution, macroscopic morphology observation revealed that the self-assembled pDA surface resulted in a darker color of the HDPE scaffold, which was attributed to the successful coating of pDA (Fig. 2e, h). However, the pDA-EFE scaffold displayed identical morphology to those of the pDA scaffold, indicating that the incorporation of LBL coatings did not influence the morphology of the composite scaffolds (Fig. 2k). In addition, the 3D microstructure of the scaffold was investigated using SEM. In the low-magnification SEM images, all scaffolds showed regular arrays with interconnected pores (Fig. 2f, i, and l). These results indicated that the scaffold had better porous connectivity and may be more suitable for tissue metabolism. Fig. 2g reveals distributed cracks on the uniform and smooth surface of the HDPE scaffold, whereas the pDA scaffold displayed a rough micromorphology, suggesting that pDA was deposited on the surface of HDPE (Fig. 2j). After the HDPE coating of LBL, the pDA coating was covered by LBL assembly coatings with particulate aggregates of EPL and a smoother FIB membrane (Fig. 2m). These results suggest changes on

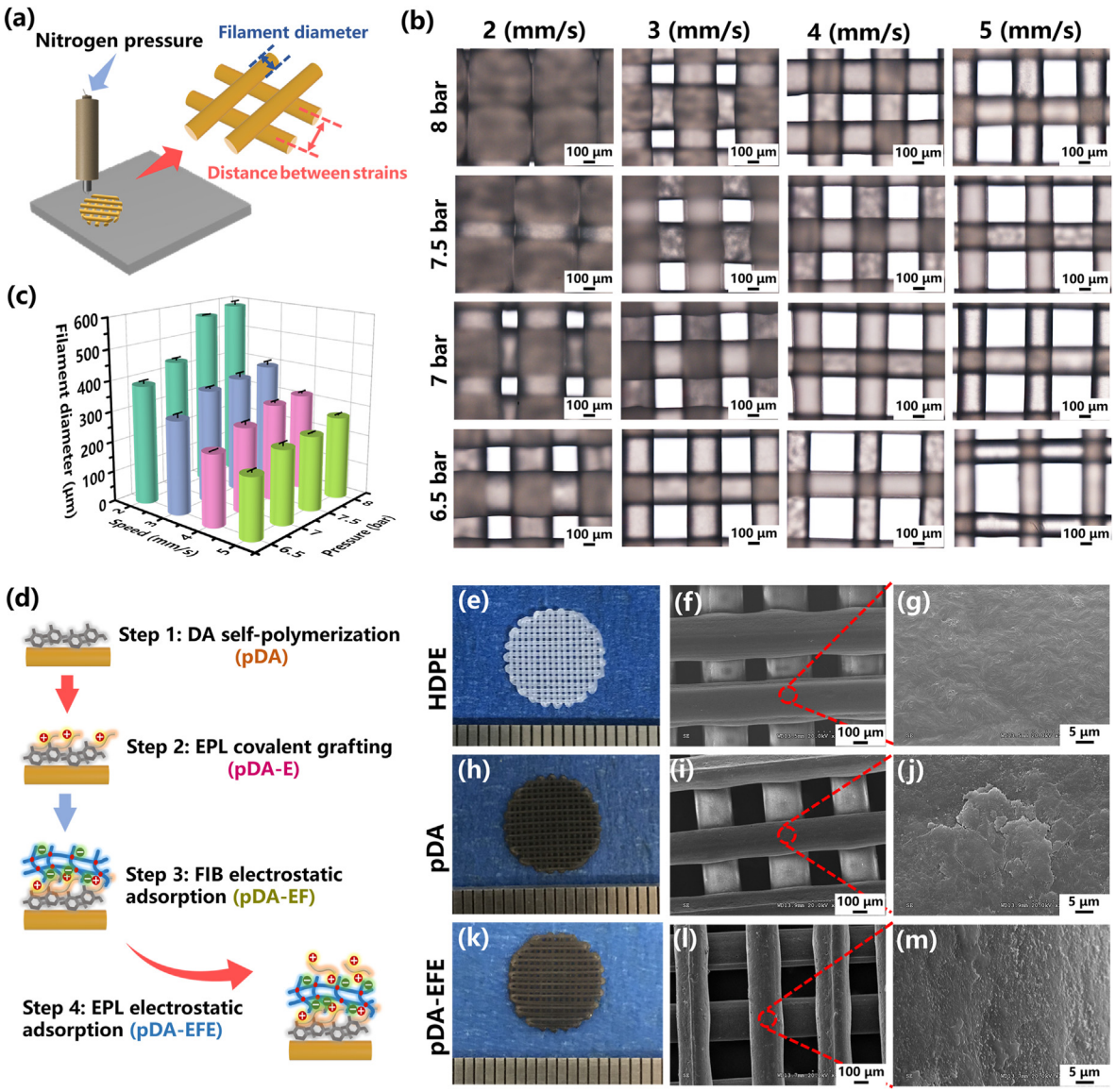

Fig. 2. Characterization of pDA-, EPL-, and FIB-modified HDPE scaffolds. (a) Schematic illustration of the preparation of different filament diameters of HDPE scaffold. (b) Optical microscopic images of filament diameter of HDPE scaffold with varying rates of speed and pressure parameters. (c) Quantitative analysis of filament diameter of HDPE scaffold. (d) Schematic diagram of the mechanism of the pDA-triggered coating with EPL and FIB. The digital photographs and corresponding SEM images of HDPE (e, f, g), pDA (h, i, j), and pDA-EFE (k, l, m) scaffolds, respectively.

the surface of HDPE and successful coating. As shown in the EDS results, except for HDPE, nitrogen (N) was detected in all other groups, especially on the surface of the pDA-EFE scaffold with a significantly increased nitrogen (N) content (Fig. S1). This result further indicates that the LBL coatings were successfully applied to the surface of the HDPE scaffolds because pDA, EPL, and FIB contain a large amount of N elements [27,35,41]. Moreover, SEM was further used to observe the static stability of LBL coating at preset times. As shown in Fig. S2, little change was found on the surface of pDA scaffold before and after immersion in DMEM for 1, 3, and 5 days. This result indicated that PDA coating had relative stability. In pDA-E, pDA-EF, and pDA-EFE groups, the surface of EPL particulate and FIB membrane slightly decreased after immersion in DMEM, which indicated that the LBL coating degrades extremely slowly in the short term. Therefore, the abovementioned results demonstrated that pDA, EPL, and FIB were successfully co-layered and adhered to the surface of HDPE scaffolds with good stability.

To further confirm the chemical elemental composition of the surfaces of the different scaffolds, XPS analyses were performed. The semiquantitative results of different scaffold surface chemical elements showed that the carbon (C) content continued to decrease with each step of the coating (Fig. 3a). These results indicate that the surface of the HDPE scaffold was gradually covered by the coating, as it contains mainly C, while the LBL coating contains a large amount of N and other elements. However, compared with that in HDPE, the N content in the pDA, pDA-E, pDA-EF, and pDA-EFE scaffolds increased, which was in accordance with the EDS results. These results verified the successful LBL coating of the HDPE scaffold. As shown by the wide scan spectra, the decrease in the intensity of the C1s peak and the presence of the N1s peak on the pDA scaffold surface indicated that pDA was successfully coated onto the HDPE surface (Fig. 3b). In addition, the presence of the gradually increasing N1s peak in the pDA-E, pDA-EF, and pDA-EFE scaffolds suggests that LBL coatings were successfully applied onto the HDPE scaffold surface. Moreover, the high-resolution XPS spectra showed new peaks after surface modification through LBL coating. The region of the C1s for scaffolds showed three overlapping peaks of C–C/C═C, C═N/C–O, and C–N/C═O, located at 284.8, 286.26, and 288.43 eV, respectively. As shown in Fig. 3c, for the pDA-E, pDA-EF, and pDA-EFE scaffolds, the C–N/C═O peak gradually increased and was higher than that

(a)

Code	O1s (%)	C1s (%)	N1s (%)
HDPE	0.03	99.97	N.A.
pDA	19.70	73.14	7.16
pDA-E	13.28	70.31	16.41
pDA-EF	18.43	66.42	15.15
pDA-EFE	17.90	66.16	15.94

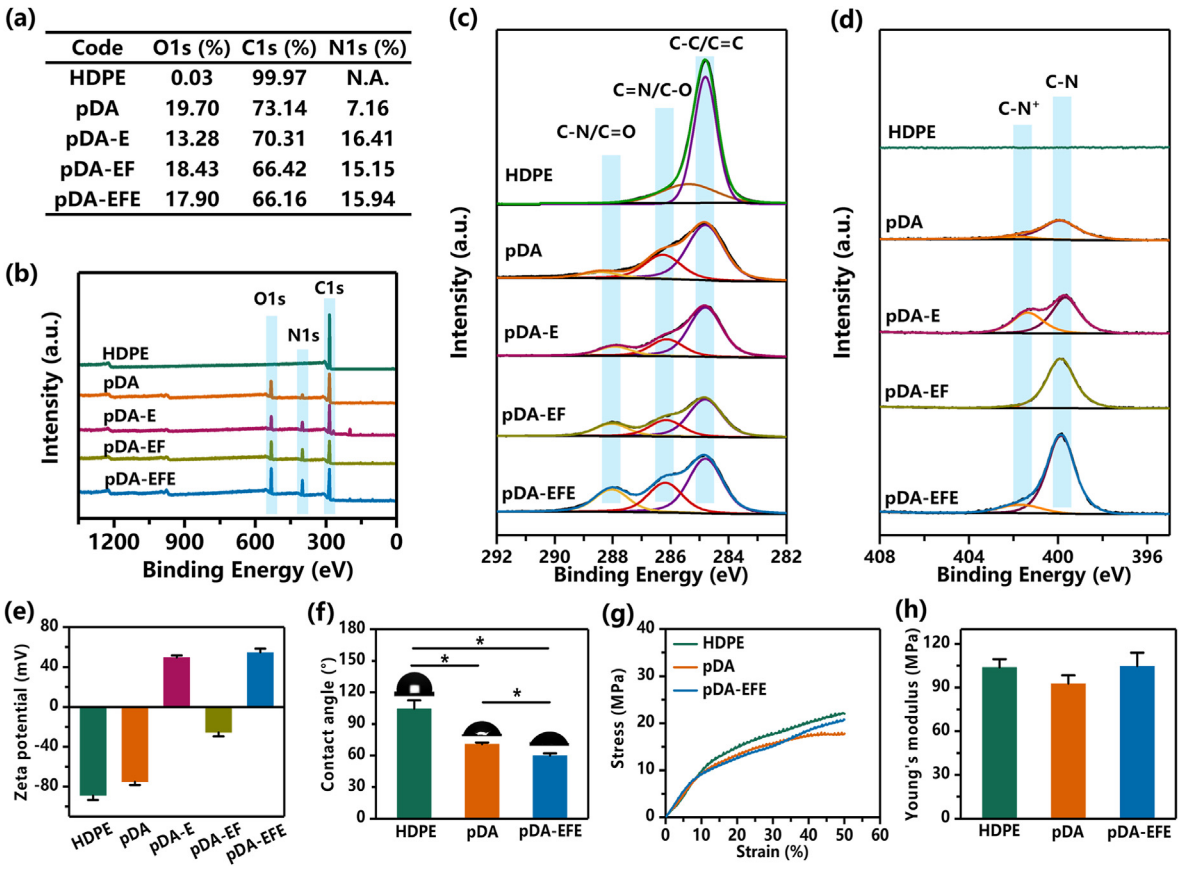

Fig. 3. Surface characterization of different scaffolds. (a) The concentration of elements is based on XPS analysis. (b) XPS survey spectra for detection of C, N, and O elements. (c–d) The high-resolution spectrum of C1s/N1s for HDPE, pDA, pDA-E, pDA-EF, and pDA-EFE scaffolds. (e) Transformation of zeta potential of HDPE functionalized with pDA, FIB, and EPL through an LBL fabrication method. (f) Water contact angle measurement. Mechanical tests show no significant difference in the scaffolds' compressive stress (g) and Young's modulus (h). ($P < 0.05$, n = 3).

of the pDA scaffold, which was attributed to the carbonyl group, suggesting the existence of EPL and FIB coatings. Moreover, the increased C–N^+ signals at 401.71 eV in the N1s XPS of the pDA-E and pDA-EFE scaffolds were in accordance with the successful grafting of EPL to pDA or pDA-EF due to the protonated amino group from EPL (Fig. 3d) [37]. Collectively, this designed coating was successfully constructed on the surface of HDPE, and this highly active pDA was grafted with LBL coatings to obtain HDPE bioactive properties.

To further explore the immobilization of LBL coatings on the HDPE surface and the association between the EPL and FIB, a zeta potential analysis was used to measure the surface potential of these scaffolds. The surface charge measurement results for each scaffold sample are shown in Fig. 3e. The HDPE scaffold surface showed the lowest zeta potential (−88.96 ± 4.44 mV), suggesting that the HDPE scaffold surface had a highly negative charge at pH 7.4. The application of the pDA scaffold decreased the zeta potential to −75.19 ± 3.23 mV, further demonstrating that the pDA scaffold was successfully coated onto the HDPE surface. Further treatments with EPL and FIB, the zeta potential of pDA-E, pDA-EF, and pDA-EFE scaffolds were +49.62 ± 2.06, −25.46 ± 4, and +54.7 ± 3.68 mV, respectively, eventually generating a positively charged surface on the substrates. Interestingly, the surface charge of each scaffold showed a wave shape, because EPL carries a large positive charge and FIB carries a small negative charge [30,43]. These results suggest that the LBL coating was successfully generated by interaction resulting from the electrostatic absorption principle [32]. The surface charge on the pDA-EFE scaffolds has a complex influence on biofilm formation and cell adhesion. Therefore, the surface of this scaffold may promote cell adhesion, because the cell membrane surface is negatively charged [30].

Controlled hydration capacity of implanted biomaterials is essential for tissue ingrowth because a hydrophilic surface of implants is favorable for cell adhesion [49]. To study the hydrophilicity of the scaffold surfaces, the WCA was measured. As shown in Fig. 3f, HDPE had a WCA angle of 105° ± 8°, indicating a typical hydrophobic surface of a polymer material with no active groups and low surface energy [50]. Further treatment with LBL coatings decreased the WCA angle of the pDA and pDA-EFE scaffolds to 71° ± 2° and 60° ± 2°, respectively, owing to the hydrophilicity of the composite coating. These results demonstrated that the modification of HDPE scaffolds with EPL and FIB incorporation by pDA coating increased their hydrophilic properties, with the abundant amino groups in pDA and EPL playing a dominant role.

Biomechanical properties are considered to be the most important features for determining the suitability of HDPE scaffolds for auricle reconstruction. Moreover, surface modification should be based on the premise of not sacrificing the original mechanical properties of the HDPE scaffold. The stress curves of the HDPE, pDA, and pDA-EFE scaffolds showed no significant differences (Fig. 3g), indicating that the pDA-EFE scaffold should still fully meet the requirements regarding their mechanical properties. A previous study has shown that biomechanical property mismatch between implants and native tissue is a major cause of seroma formation and partial or total extrusion of the implants, while 3D printed HDPE scaffolds can ameliorate this situation [45]. As shown in Fig. 3h, the Young's modulus of the HDPE (103.78 ± 5.74 MPa), pDA (92.65 ± 5.71 MPa), and pDA-EFE (104.7 ± 9.21 MPa) scaffolds were approximated. Although these 3D printed scaffolds still showed the higher modulus compared with natural auricular cartilage (5.02 ± 0.17 MPa), the modulus of these scaffold were significantly lower than that of Medpor® (140.9 ± 0.04 MPa) due to the controllable 3D printing porous structure [13]. Thus, these results indicate that their biomechanical

properties are not affected by the coating and are more competitive than those of the clinically used Medpor®. In addition, the porous 3D structure of HDPE showed excellent mechanical performance and could support the auricle shape for a long time and provide lower stress to reduce the ulceration rate of auricle skin.

3.2. Cytocompatibility and cellular behavior of L929 cells on pDA-EFE scaffolds

To evaluate the *in vitro* biocompatibility of these scaffolds, L929 cells were seeded onto all scaffold groups and further cultured to investigate the cellular viability (Fig. 4a). The live/dead fluorescence assay results showed that most of the L929 cells in the HDPE, pDA, and pDA-EFE groups were stained green, indicating that the cells were living (Fig. 4b–j, Fig. S4). These results showed a significant difference in the number of cells observed between the HDPE and coating groups, which indicated that these treated samples showed more cell adhesion than the HDPE group. Further quantitative evaluation revealed no visible difference in cell viability between pure and modified HDPE after 3 days of culture (Fig. 4k), suggesting their excellent cytocompatibility with L929. In addition, the proliferation of L929 cells on all scaffold groups was measured using the alamarBlue reagent. To compare the changes in fluorescence intensity, all scaffold groups were subjected to quantitative analysis after being cultured for 1, 3, and 5 days. On days 1 and 3, the fluorescence of pDA and pDA-EFE groups were significantly higher than that of the HDPE group, demonstrating that both the pDA and EFE functional coatings were able to promote cell proliferation. In contrast, cells in the pDA-EFE group showed the highest fluorescence intensity on day 5, indicating a higher cell growth rate of the pDA-EFE group compared with that of the other groups (Fig. 4l), which is mainly due to the promising ability of FIB to promote the proliferation of fibroblasts [34]. It is well known that ordinary antibiotic coatings (such as AgNPs, and QACs) have a good spectral antibacterial ability, while the potential cytotoxicity of these antibiotic materials should be considered [38]. In contrast, the previous studies have demonstrated that the EPL not only showed the excellent antibacterial ability but also has good biocompatibility [30,31]. Therefore, EPL was chosen as the coating material for developing the PDA-EFE scaffolds, which showed relatively strong antibacterial and biocompatibility properties. In addition, the incorporation of pDA, EPL, and FIB, such as hydroxyl, amino cation, carboxyl, and RGD groups on the surface of HDPE scaffolds, could enhance the hydrophilicity and provide binding sites, and cell adhesion and proliferation were increased with the extension of incubation time [27,33,51]. Therefore, LBL coatings could provide a desirable microenvironment for cell attachment and proliferation, laying the foundation for tissue regeneration.

Fluorescence staining was further performed to analyze the cellular morphologies of L929 cells in these scaffold groups, where phalloidin–FITC and DAPI were used to observe the cytoskeleton and nucleus, respectively. After 3 days of cultivation, cell morphology on all scaffolds was observed and analyzed. Through the side view of the scaffold, it was divided into two layers to analyze the distribution of L929 cells separately (Fig. 5j). The top and 3D views of the fluorescent staining images revealed that L929 cells in pDA and pDA-EFE groups were evenly

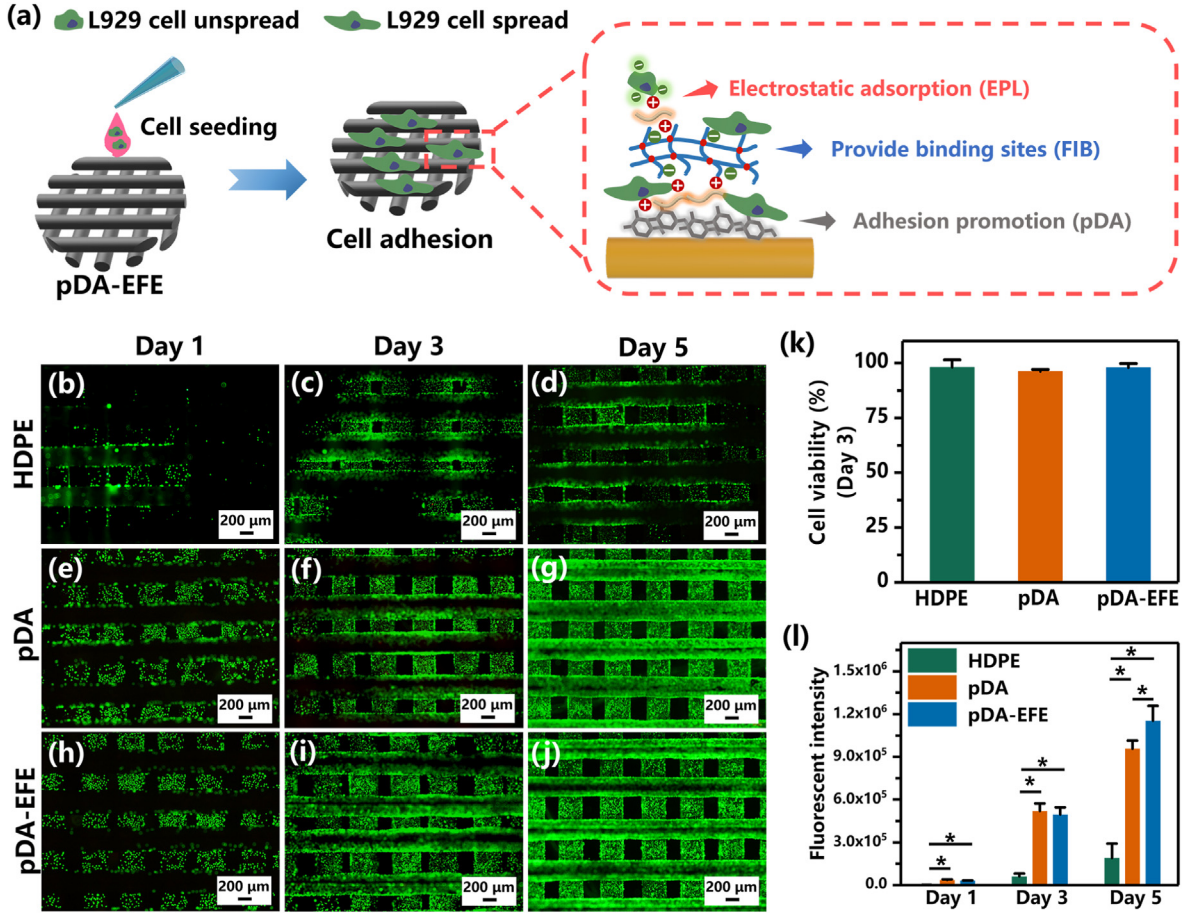

Fig. 4. The cellular viability and proliferation of L929 on scaffolds. (a) Scheme of L929 cells seeded and cultured on scaffolds. Live/dead staining fluorescence images of L929 cells on HDPE (b–d), pDA (e–g), and pDA-EFE (h–j) scaffolds after culturing for 1, 3, and 5 days. (k) Relative cell viability percentages of L929 cells on scaffolds after culturing for 3 days, which were evaluated by live/dead assay. (l) The proliferation analysis of L929 cells on scaffolds based on fluorescence intensity analysis *via* alamarBlue viability reagent. ($P < 0.05$, n = 3).

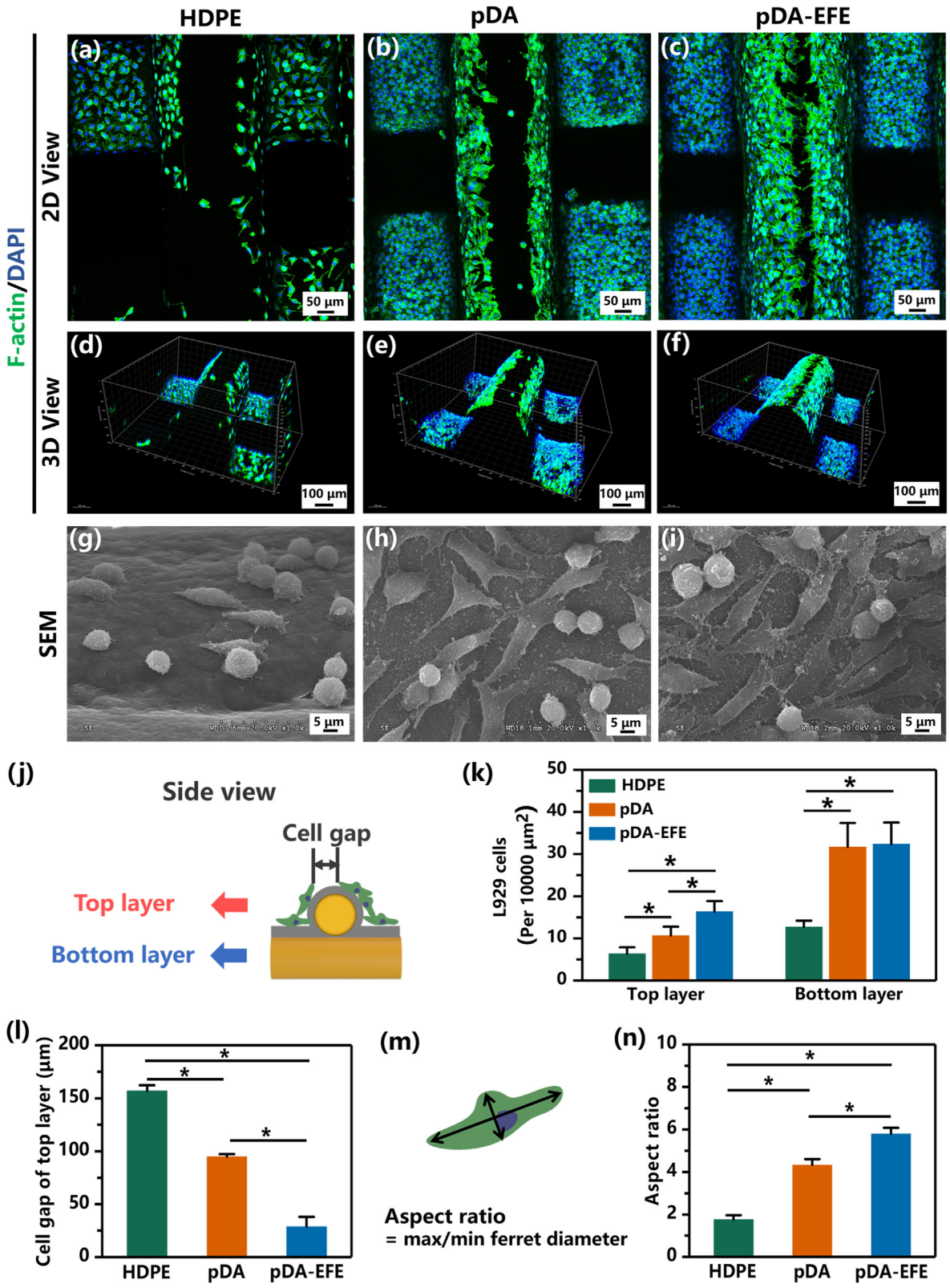

Fig. 5. The morphological analysis of L929 cells cultivation with scaffolds after culturing for 3 days. The top views and 3D views of the confocal fluorescence microscopy images of L929 cells on HDPE (a, d), pDA (b, e), and pDA-EFE (c, f) scaffolds stained with F-actin (green) and DAPI (blue). The SEM images of L929 cells spreading on HDPE (g), pDA (h), and pDA-EFE (i) scaffolds. (j) Schematic diagram of the distribution of L929 cells on the scaffolds. (k) Quantitative analysis of the number of L929 cells on the top layer and under the layer of the scaffolds. (l) Quantitative analysis of cell gap on the top layer of the scaffolds. (m) The scheme of cellular elongation by measuring the cellular aspect ratio. (n) The statistical analysis of cellular aspect ratios of L929 cells on HDPE, pDA, and pDA-EFE scaffolds. ($P < 0.05$, n = 3).

distributed and fully adhered to the surface of the scaffolds; however, the L929 cells in the HDPE group had an inadequate spread and were not as well adhered as in the pDA or pDA-EFE groups (Fig. 5a–f, Figs. S5–6). These results further demonstrated that the bioactive coating significantly promoted L929 cell adhesion, which was in accordance with the live/dead staining outcome. Further quantification evaluation showed that more cells were attached to the top layer of the surface than to the bottom layer (Fig. 5k). Moreover, the cell gap gradually narrowed on the top layer with the LBL coating (Fig. 5l). All these results imply that the pDA-EFE group had better cell adhesion performance than the pDA group due to the electrostatic adsorption of EPL on cells and the binding sites provided by FIB. Sequentially, the SEM images revealed that L929 cells were extended pseudopods and fully spread on the scaffold surfaces of the pDA and pDA-EFE groups (Fig. 5g–i, Fig. S7). In contrast, L929 cells cultured on HDPE remained round and showed no extended pseudopods. These results demonstrated that the pDA-EFE group possessed excellent *in vitro* cell adhesion and proliferation properties. Based on the SEM images, the elongation of L929 cells on all scaffold samples was quantitatively analyzed based on the cellular aspect ratio, which is defined as the ratio between the longest and shortest cell length across the nuclei (Fig. 5m) [44]. As shown in Fig. 5n, the cellular aspect ratios of the pDA and pDA-EFE groups were as high as 4.33 ± 0.28 and 5.79 ± 0.29, respectively, while the aspect ratio of the HDPE group was only 1.76 ± 0.2. In particular, the pDA-EFE group showed a higher aspect ratio than the HDPE group, which further indicated that the bioactive coating process boosted the spread and adherence of L929 cells. The above-mentioned results suggest great potential of multifunctional-coated HDPE scaffolds for promoting skin tissue ingrowth.

3.3. *In vitro* bacteriostatic assays

Bacterial colonization and biofilm formation on implants have been a challenge for the medical community [38]. In the present study, gram-positive *S. aureus* (the most common pathogen in implant infections) and gram-negative *E. coli* were selected to verify the antibacterial properties of the pDA-EFE scaffold (Fig. 6a) [52,53]. An SYTO-9/PI

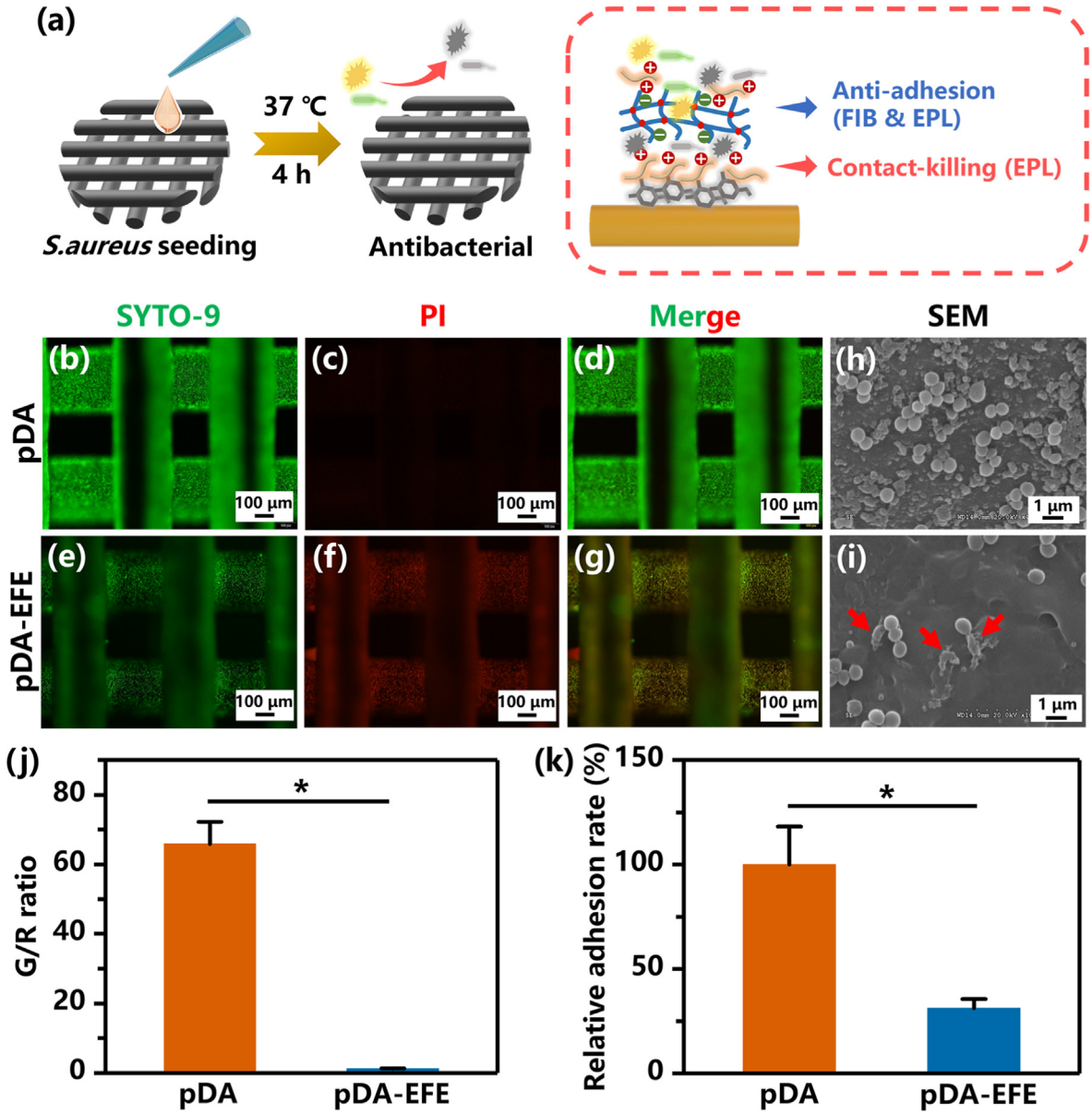

Fig. 6. Antibacterial effects of pDA and pDA-EFE scaffolds. (a) Schematic illustration of *in vitro* antibacterial experiment and principle. SYTO-9/PI analysis of *S. aureus* viability on pDA (b–d) and pDA-EFE (e–g) scaffolds with corresponding quantity analysis (j). SEM images of *S. aureus* attached on pDA (h) and pDA-EFE (i) scaffolds with corresponding quantity analysis (k). ($P < 0.05$, n = 3).

assay was performed to determine the antibacterial activity of the pDA-EFE scaffold. The green fluorescent nucleic acid dye SYTO-9 was used to stain both live and dead bacteria, whereas dead cells were dyed only by red-fluorescent nucleic acid dye PI base on PI could only penetrate through the ruptured cell membrane. As displayed in Fig. 6b–g and Fig. S8, *S. aureus* and *E. coli* on the pDA scaffold mostly survived, whereas those on the pDA-EFE group mostly died. In addition, a quantification analysis revealed that the positive area ratio of green/red (G/R) of *S. aureus* in the pDA-EFE scaffold was significantly lower than that in the pDA scaffold (Fig. 6j). These findings implied that the pDA scaffold was unable to inhibit the growth of bacteria, whereas the LBL coatings enhanced the antibacterial activity of pDA coating for inhibiting the growth of *S. aureus*. Next, to obtain insights into the antibacterial activity of the pDA-EFE scaffolds, the morphology of the *S. aureus* was observed using SEM. The *S. aureus* on the pDA-EFE scaffolds exhibited rough surfaces with cellular deformation and membrane degradation (red arrows), whereas the *S. aureus* on the pDA scaffolds exhibited a smooth spherical shape with regular morphology (Fig. 6h and i). This can be explained by the positive charge of the EPL interfering with the bacterial cell membrane or hindering the normal metabolic activity of the bacterial cells, resulting in the rupture of bacterial cell membranes and the prevention of bacterial growth and reproduction [35]. Further quantification evaluation showed that *S. aureus* was less abundant on the surface of the pDA-EFE scaffold than on the pDA scaffold (Fig. 6i, Fig. S9), indicating that the pDA-EFE scaffold resisted bacterial adhesion. A previous study demonstrated that FIB can inhibit the initial stage of bacterial adhesion because of its surface perturbation function [54]. Therefore, we hypothesized that EPL and FIB bound by electrostatic adsorption would dissolve slowly into the nutrient solution during bacterial culture, leading to a decrease in the number of bacteria attached to the pDA-EFE scaffold. These results suggested that the pDA-EFE scaffold has superior antibacterial and antibacterial adhesion properties compared to the pDA scaffold, which may help to prevent HDPE implant-associated infections.

3.4. *In vivo alleviate inflammatory response and antibacterial performance of pDA-EFE scaffolds*

In addition to bacterial infections, the host foreign body response induced by implants is another complication [25,55]. In this study, we subcutaneously implanted pDA-EFE scaffolds into SD rats to determine their alleviating inflammatory response and antibacterial properties *in vivo* (Fig. 7a). It is well known that the appearance of inflammatory cells suggests an early foreign body response or bacterial infection [56]. H&E staining can show obvious inflammatory cells (neutrophils and lymphocytes), and CD68 is a typical cell surface marker of inflammatory macrophages [30,56]. After implantation for 7 days, intense inflammatory cell infiltration induced by the foreign body response and *S. aureus* infection was observed in the HDPE and pDA-S scaffolds (Fig. 7b, Figs. S10–11). In contrast, pDA, pDA-EFE, and pDA-EFE-S scaffolds showed milder cell infiltration, suggesting effective alleviating inflammatory and antibacterial properties of pDA, FIB, and EPL, respectively. Interestingly, the inflammatory reaction of the pDA-EFE-S scaffold was slightly higher than that of the pDA-EFE scaffold, even with minor bacterial infection, and the quantification analysis revealed fewer inflammatory cells at the implanted sites of the pDA-EFE-S scaffold (Fig. 7d). These results of CD68 immunofluorescence staining are consistent with the H&E images and quantitative results, further indicated that the LBL coatings have obvious alleviating inflammatory and antibacterial effects. After implantation for 14 days, the number of inflammatory cells in the HDPE and pDA-S scaffolds decreased but was significantly higher than those in the other scaffold groups (Fig. 7c, Figs. S10–11), which was also in accordance with the outcome of quantification analysis (Fig. 7f). These results suggested that the HDPE and pDA-S scaffolds had a relatively strong inflammatory effect during the non-acute inflammatory phase. In addition, these results also demonstrated the capacity of the LBL-coated implant to significantly limit the risk of implant-associated bacterial colonization and infection. Therefore, this technology might provide an important novel strategy for reducing the risk of implant infection, along with excellent *in vivo* tissue reconstruction.

3.5. *Morphology analysis and in vivo evaluation of auricle-shaped scaffolds*

The relative ease of implantation and anatomical accuracy make 3D-printed bioscaffolds an appealing alternative for auricular reconstruction [57,58]. Therefore, this study evaluated the histocompatibility of LBL coatings on HDPE (auricle) scaffolds *in vivo*. First, to test the accuracy of the 3D printing technology, the original auricle model was compared with an HDPE auricle scaffold to evaluate the shape similarity. As shown in Fig. 8b, the color map shows the deviation of the auricle scaffold from its original shape, with red/orange designating high deviation and green/blue designating low deviation. These results revealed that the shape of the HDPE auricle scaffold was similar to that of the original model, with a deviation of <1 mm. Therefore, we concluded that accurate shape control of the scaffold was achieved using the 3D printing technology.

Herein, the auricle-shaped model was divided into two parts: high displacement (HD, marked by the red area) and low displacement (LD, marked by the blue area), by finite element analysis, represented by higher and lower stress areas, corresponding to the amount of local stress on the skin (Fig. 8c). After implantation for 28 days, the tissue sections were stained by H&E, CD68, and DAPI staining (Fig. 8d. Fig. 8e). Interestingly, almost all HDPE auricular scaffold groups displayed skin tissue ingrowth, indicating that the porous structure of 3D printed HDPE is suitable for tissue ingrowth. Additionally, these results also showed higher numbers of inflammatory cells adhered to the pores of HDPE auricle scaffolds (especially in the HD area), compared to pDA-EFE auricle scaffolds. These quantitative results are consistent with the H&E, CD68, and DAPI images, showing that fewer inflammatory cells adhered to the pDA-EFE auricle scaffold (Fig. 8f and g), indicating their satisfactory alleviating inflammatory properties. Localized stress concentrations at the skin-implant interface may lead to micromotion and detachment of implant cell/protein binding sites due to the differential loading and may thus increase the chance of infection, leading to implant extrusion [59]. Therefore, we can assume that the porous structure of the pDA-EFE (auricle) was suitable for skin tissue ingrowth with a certain ability to resist foreign body reactions and local stress inflammation owing to the porosity of the 3D printed scaffold and the alleviating inflammatory and pro-repair properties of the LBL coatings. The results of this *in vivo* experiment show that the 3D printing and LBL coating technique used in this study could reduce some of the complications associated with implants.

Collagen is the principal component of skin tissue, and its content is a critical index that reflects the activity of fibroblasts [60]. Therefore, Sirius red staining was used to detect the sections of all scaffold samples in this study. As shown in Fig. 9a, the pDA-EFE (auricle) scaffold showed higher collagen content in both the HD and LD areas, indicating that it had the most significant collagen production, consistent with the quantitative analysis (Fig. 9c), which implied better tissue integration. These results further illustrated that skin tissue could grow into porous auricle scaffolds, which is consistent with previous H&E staining results. However, implant surface properties play an important role in collagen deposition because tissues first come into contact with the surface [60]. Therefore, the results of this study suggested that the pDA-EFE auricle scaffold surface is more suitable for collagen deposition and tissue ingrowth due to its porous structure and the biofunctional activity of the LBL coatings.

Vascularization of porous implants is particularly important for promoting tissue ingrowth [61]. To investigate angiogenesis during skin tissue ingrowth, immunofluorescence staining of the endothelial marker CD31 and the vascular smooth muscle marker α-SMA was performed during the formation of new blood vessels. On day 28, the

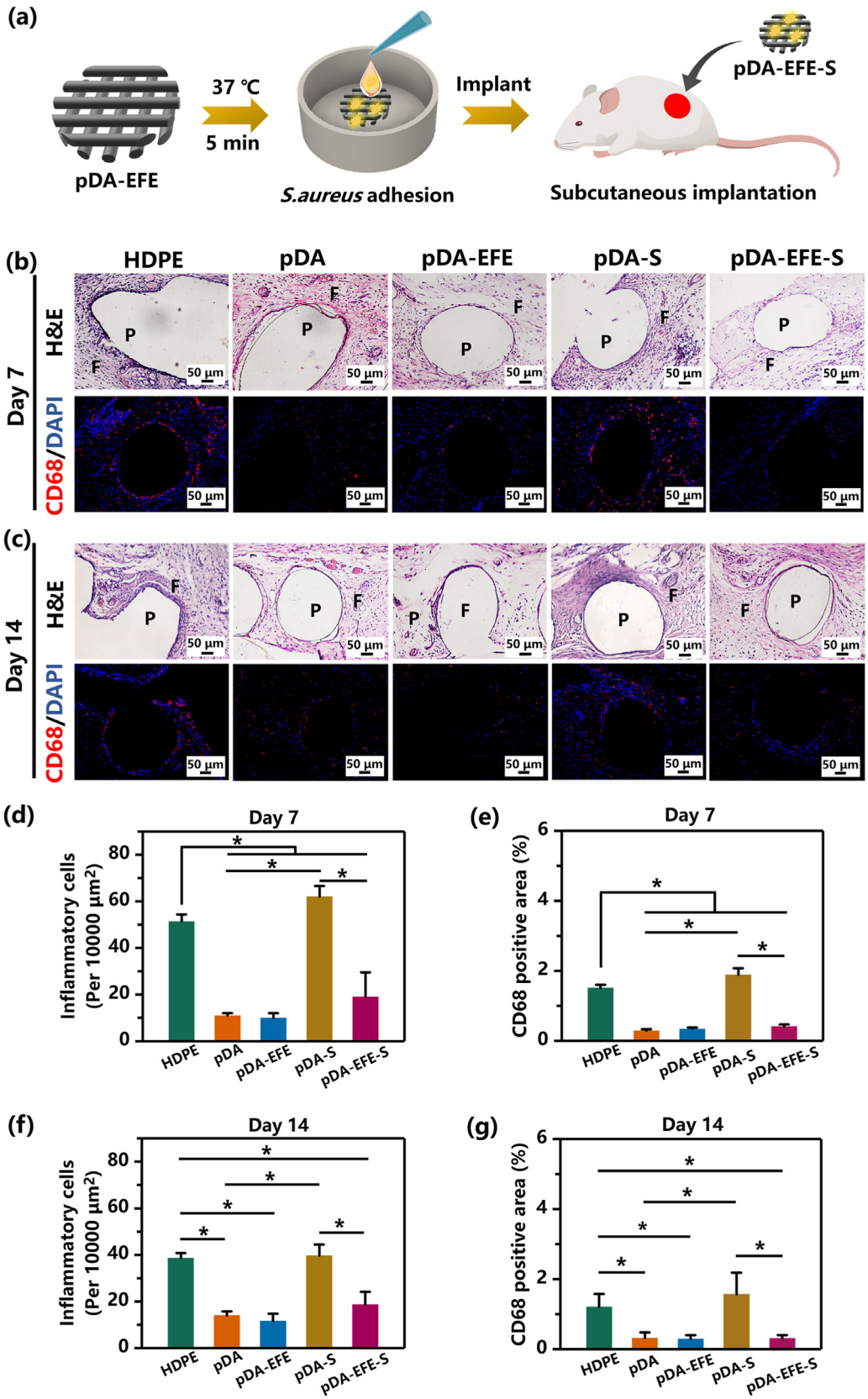

Fig. 7. *In vivo* histocompatibility and antibacterial activity evaluation of pDA-EFE scaffold in the rat model. (a) Schematic diagram of the implantation method. Representative images of H&E, CD68 (red), and DAPI (blue) -stained sections of subcutaneously implanted scaffolds with surrounding tissues (b, c). Samples were harvested at 7- and 14-days following implantation. (P = polymer, and F = fibrous inflammatory zone). The statistical data of the abundance of inflammatory cells on days 7 (d, e) and 14 (e, g). ($P < 0.05$, n = 3).

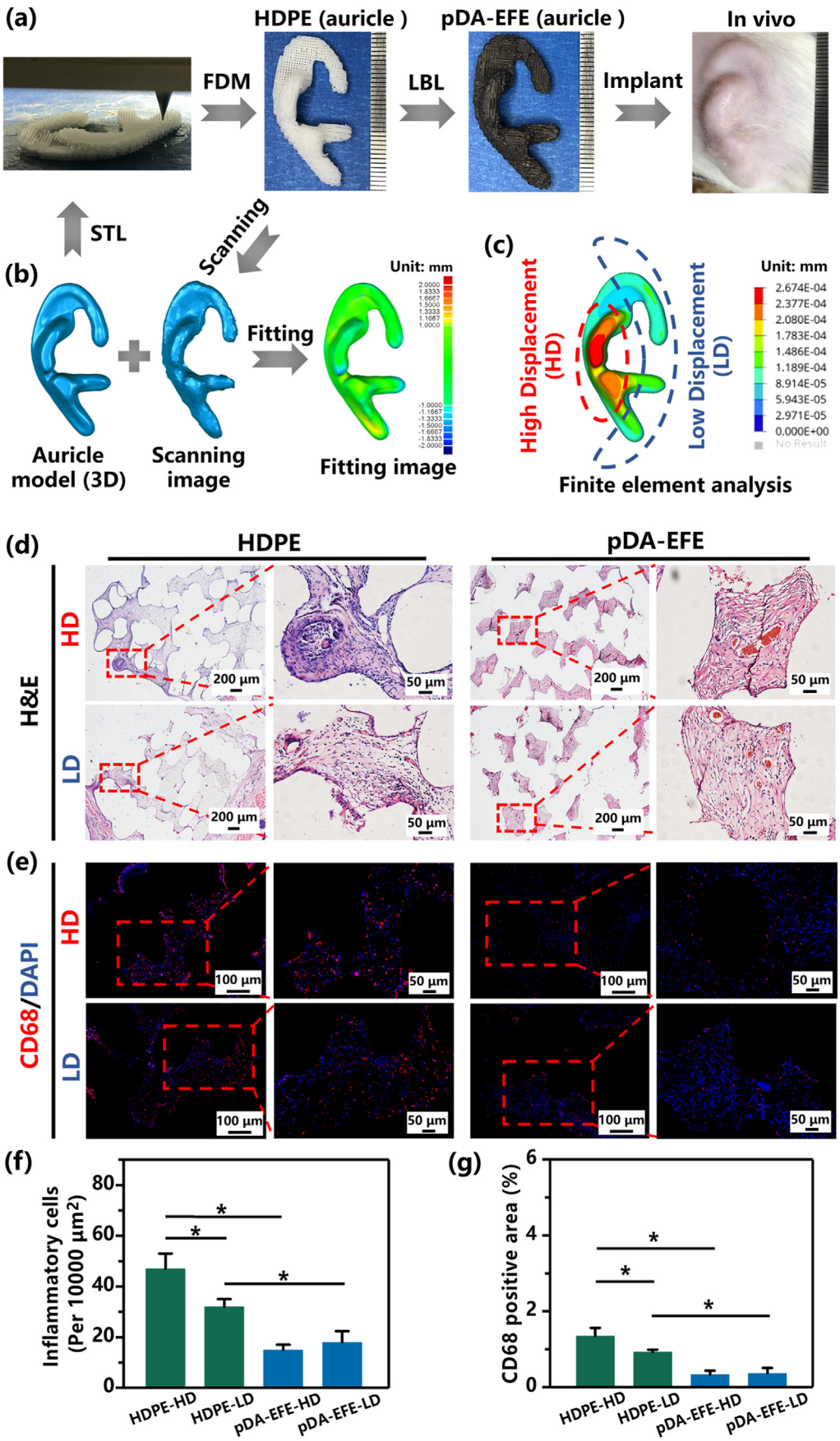

Fig. 8. Preparation of HDPE (auricle) scaffolds for implanted evaluation. (a) Schematic illustration of the HDPE (auricle) scaffolds preparation process and implantation method. (b) Laser scanning confirms that the printing accuracy of the HDPE (auricle) scaffolds. (c) Finite element analysis-based prediction of the displacement gradient distribution in the original model. (d) H&E-stained images of samples after 28 days, and the statistical data of inflammatory cells (f). Fluorescence images of CD68 (red) and DAPI (blue) staining (e) and quantitative analysis (g). ($P < 0.05$, n = 3).

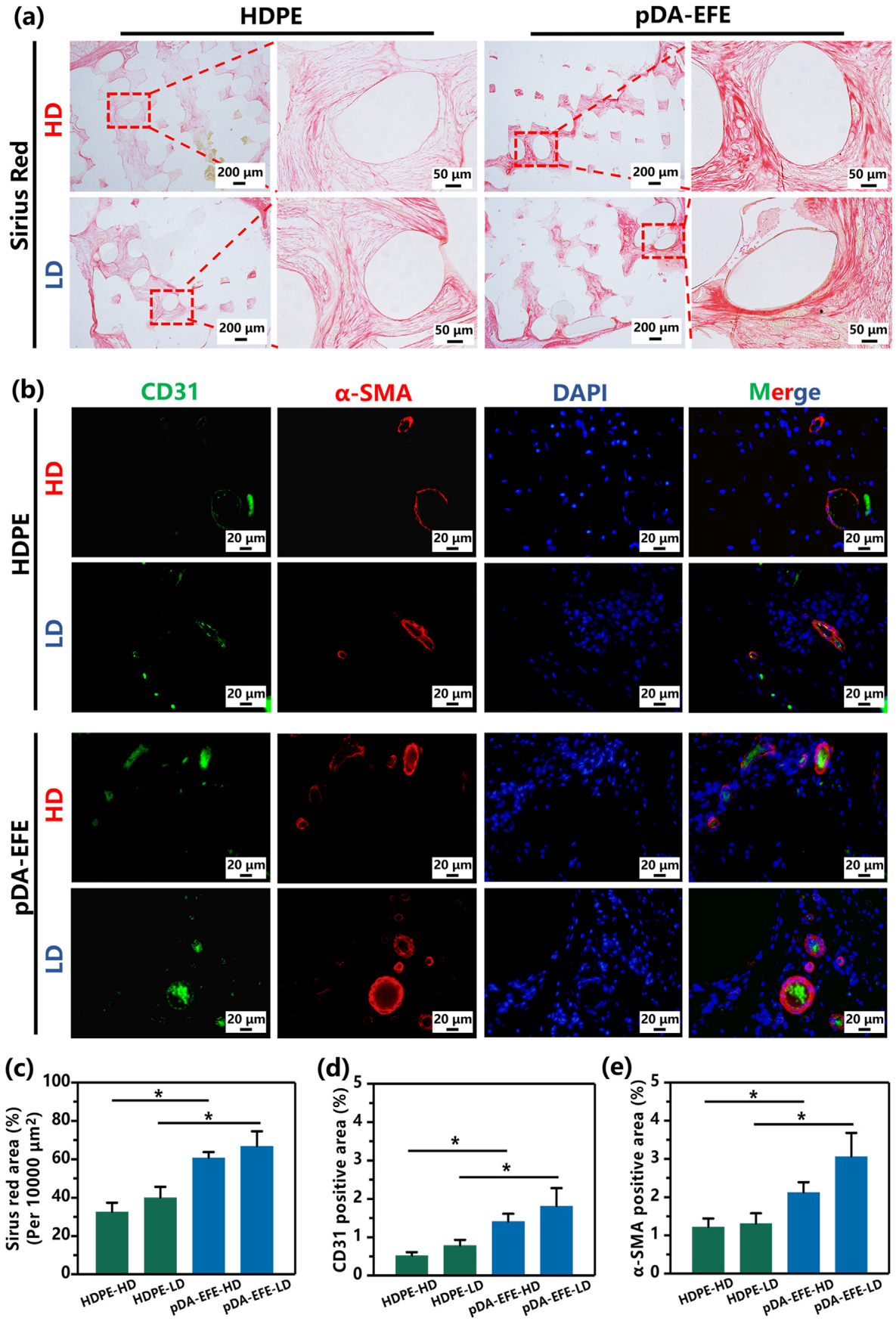

Fig. 9. Representative immunofluorescence staining at 28 days. Sirius red images (a) and quantitative analysis (c). (b) Fluorescence images of CD31 (green), α-SMA (red), and cell nucleus (blue) staining. (d, e) Quantitative analysis of positively stained areas using ImageJ software. ($P < 0.05$, n = 3).

vessel-occupied area indicated that the expression of CD31 and α-SMA in the pDA-EFE auricle scaffold was significantly higher than that in the HDPE auricle scaffold (Fig. 9b), and no apparent difference was observed between HD and LD (Fig. 9d and e). These *in vivo* results demonstrated that the multifunctional LBL coatings possess antibacterial and alleviating inflammatory properties and significantly promote vascularization in tissues, leading to modulation of the tissue ingrowth response.

To sum up, the traditional commercial Medpor® showed the drawbacks such as relative higher Young's modulus, the lack of bioactivity, the difficulty to match individual design, which would lead to the easy infection and ulcer in clinical application. Therefore, in this study, we developed the pDA-EFE auricle scaffold using 3D printing technique, and further modified these scaffold with bioactive and antibacterial properties using the LBL surface modification approach to overcome these shortcoming. The 3D printed auricle implants had revealed that the pDA and EFE decorated porous HDPE had the following characteristics: personalizable, excellent bioactive, antibacterial, improved vascularization, and tissue ingrowth. However, more works are required before realizing its actual application in the clinic. Among them, exploring the influence of biomechanical on the implant tissue integration from the optimized structure and verifying the effectiveness of the implant *via* a long-term animal auricle repair model is of uppermost priority, which will also be carried out in our future work.

4. Conclusion

In summary, we successfully developed a 3D printable porous HDPE auricle scaffold with self-assembled LBL coatings that possess synergistic functions. We found that the LBL-coated HDPE auricle scaffolds have individualized structural features and satisfactory surface biofunctional activity. In addition, they were found to facilitate the ingrowth of skin tissue and may function better than traditional commercial auricular implants. Furthermore, the pDA-EFE scaffolds showed antibacterial and cytocompatibility properties, as well as excellent antibacterial activity against *E. coli* and *S. aureus*. In addition, the developed scaffolds promoted the adhesion, spread, and proliferation of L929 cells *in vitro*. The pDA-EFE and pDA-EFE auricle scaffolds also exhibited outstanding antibacterial ability, satisfactory biocompatibility, weaker inflammatory reaction, alleviation of stress damage, and better auricles in both the normal and infectious environments in a rat model. Due to the simple preparation process and biosafety of raw biomaterials, 3D printing technology and the LBL coating method may have broad application potential in the manufacturing and surface modification of various types of implants for clinical applications.

Credit author statement

Junfeiyang Yin: Conceptualization, Methodology, Data curation, Formal analysis, Writing-Original draft preparation. **Jing Zhong:** Conceptualization, Methodology. **Jiejie Wang:** Conceptualization, Methodology, Review & Editing. **Yilin Wang:** Review & Editing. **Ting Li:** Review & Editing. **Ling Wang:** Methodology. **Yang Yang:** Review & Editing. **Zhifang Zhen:** Review & Editing. **Yanbing Li:** Review & Editing. **Hongwu Zhang:** Review & Editing. **Shizhen Zhong:** Review & Editing, Surpervision. **Yaobin Wu:** Conceptualization, Review & Editing, Surpervision. **Wenhua Huang:** Conceptualization, Surpervision, Funding acquisition.

Declaration of competing interest

The authors declare that they have no known competing financial interests or personal relationships that could have appeared to influence the work reported in this paper.

Acknowledgments

This work was supported by the National Natural Science Foundation of China (31972915), the Science and Technology Project of Guangdong Province (2018B090944002), the Guangdong Basic and Applied Basic Research Foundation (2020B1515120001, 2021A1515410010), and the Supported by Southwest Medical University High-Level Talents (Zhong Shizhen Team) Special Support Program.

Appendix A. Supplementary data

Supplementary data to this article can be found online at https://doi.org/10.1016/j.mtbio.2022.100361.

References

[1] D.V. Luquetti, C.L. Heike, A.V. Hing, M.L. Cunningham, T.C. Cox, Microtia: epidemiology and genetics, Am. J. Med. Genet. 158 (1) (2012) 124–139.
[2] K. Deng, L. Dai, L. Yi, C. Deng, X. Li, J. Zhu, Epidemiologic characteristics and time trend in the prevalence of anotia and microtia in China, Birth Defects Res. A 106 (2) (2016) 88–94.
[3] G.H. Wilkes, J. Wong, R. Guilfoyle, Microtia reconstruction, Plast. Reconstr. Surg. 134 (3) (2014) 464–479.
[4] A. Shanbhag, H.I. Friedman, J. Augustine, A.F. von Recum, Evaluation of porous polyethylene for external ear reconstruction, Ann. Plast. Surg. 24 (1) (1990) 32–39.
[5] Z.M. Jessop, M. Javed, I.A. Otto, E.J. Combellack, S. Morgan, C.C. Breugem, C.W. Archer, I.M. Khan, W.C. Lineaweaver, M. Kon, J. Malda, I.S. Whitaker, Combining regenerative medicine strategies to provide durable reconstructive options: auricular cartilage tissue engineering, Stem Cell Res. Ther. 7 (2016) 19.
[6] T. Wellisz, Clinical experience with the medpor porous polyethylene implant, Aesthetic Plast. Surg. 17 (4) (1993) 339–344.
[7] K. Ali, J.G. Trost, T.A. Truong, R.J. Harshbarger, Total ear reconstruction using porous polyethylene, Semin. Plast. Surg. 31 (3) (2017) 161–172.
[8] J.S. Lim, M.S. Kook, S. Jung, H.J. Park, S.H. Ohk, H.K. Oh, Plasma treated high-density polyethylene (HDPE) medpor implant immobilized with rhBMP-2 for improving the bone regeneration, J. Nanomater. 2014 (2014) 1–7.
[9] K. Agrawal, R. Shrotriya, Management of complications of Medpor® implants in rhinoplasty, Plast. Aesthet. Res. 4 (3) (2017) 54–56.
[10] T. Spater, A.L. Tobias, M.M. Menger, R.M. Nickels, M.D. Menger, M.W. Laschke, Biological coating with platelet-rich plasma and adipose tissue-derived microvascular fragments improves the vascularization, biocompatibility and tissue incorporation of porous polyethylene, Acta Biomater. 108 (2020) 194–206.
[11] M.W. Laschke, V. Augustin, S. Kleer, T. Tschernig, M.D. Menger, Locally applied macrophage-activating lipopeptide-2 (MALP-2) promotes early vascularization of implanted porous polyethylene (Medpor(R)), Acta Biomater. 10 (11) (2014) 4661–4669.
[12] N.C. Paxton, J. Dinoro, J. Ren, M.T. Ross, R. Daley, R. Zhou, K. Bazaka, R.G. Thompson, Z. Yue, S. Beirne, D.G. Harkin, M.C. Allenby, C.S. Wong, G.G. Wallace, M.A. Woodruff, Additive manufacturing enables personalised porous high-density polyethylene surgical implant manufacturing with improved tissue and vascular ingrowth, Appl. Mater. Today 22 (2021), 100965.
[13] L. Nayyer, M. Birchall, A.M. Seifalian, G. Jell, Design and development of nanocomposite scaffolds for auricular reconstruction, Nanomedicine 10 (1) (2014) 235–246.
[14] Z. Wang, L. Wang, T. Li, S. Liu, B. Guo, W. Huang, Y. Wu, 3D bioprinting in cardiac tissue engineering, Theranostics 11 (16) (2021) 7948–7969.
[15] C.Y. Liaw, M. Guvendiren, Current and emerging applications of 3D printing in medicine, Biofabrication 9 (2) (2017), 024102.
[16] M.H. Michalski, J.S. Ross, The shape of things to come: 3D printing in medicine, JAMA 312 (21) (2014) 2213–2214.
[17] K. Hara, E. Hellem, S. Yamada, K. Sariibrahimoglu, A. Molster, N.R. Gjerdet, S. Hellem, K. Mustafa, M.A. Yassin, Efficacy of treating segmental bone defects through endochondral ossification: 3D printed designs and bone metabolic activities, Mater. Today Bio. 14 (2022), 100237.
[18] N. Nagarajan, A. Dupret-Bories, E. Karabulut, P. Zorlutuna, N.E. Vrana, Enabling personalized implant and controllable biosystem development through 3D printing, Biotechnol. Adv. 36 (2) (2018) 521–533.
[19] J.Y. Lee, B. Choi, B. Wu, M. Lee, Customized biomimetic scaffolds created by indirect three-dimensional printing for tissue engineering, Biofabrication 5 (4) (2013), 045003.
[20] J. Suwanprateeb, F. Thammarakcharoen, V. Wongsuvan, W. Chokevivat, Development of porous powder printed high density polyethylene for personalized bone implants, J. Porous Mater. 19 (5) (2011) 623–632.
[21] P. Jeyachandran, S. Bontha, S. Bodhak, V.K. Balla, M. Doddamani, Material extrusion additive manufacturing of bioactive glass/high density polyethylene composites, Compos. Sci. Technol. 213 (2021), 108966.
[22] N.C. Paxton, M.C. Allenby, P.M. Lewis, M.A. Woodruff, Biomedical applications of polyethylene, Eur. Polym. J. 118 (2019) 412–428.
[23] Z. Zheng, M. Li, P. Shi, Y. Gao, J. Ma, Y. Li, L. Huang, Z. Yang, L. Yang, Polydopamine-modified collagen sponge scaffold as a novel dermal regeneration

template with sustained release of platelet-rich plasma to accelerate skin repair: a one-step strategy, Bioact. Mater. 6 (8) (2021) 2613–2628.
[24] Z. Zhu, Q. Gao, Z. Long, Q. Huo, Y. Ge, N. Vianney, N.A. Daliko, Y. Meng, J. Qu, H. Chen, B. Wang, Polydopamine/poly(sulfobetaine methacrylate) Co-deposition coatings triggered by CuSO4/H2O2 on implants for improved surface hemocompatibility and antibacterial activity, Bioact. Mater. 6 (8) (2021) 2546–2556.
[25] X. Xu, Y. Li, L. Wang, Y. Li, J. Pan, X. Fu, Z. Luo, Y. Sui, S. Zhang, L. Wang, Y. Ni, L. Zhang, S. Wei, Triple-functional polyetheretherketone surface with enhanced bacteriostasis and anti-inflammatory and osseointegrative properties for implant application, Biomaterials 212 (2019) 98–114.
[26] X. Liu, W. Chen, B. Shao, X. Zhang, Y. Wang, S. Zhang, W. Wu, Mussel patterned with 4D biodegrading elastomer durably recruits regenerative macrophages to promote regeneration of craniofacial bone, Biomaterials 276 (2021), 120998.
[27] H.C. Yang, R.Z. Waldman, M.B. Wu, J. Hou, L. Chen, S.B. Darling, Z.K. Xu, Dopamine: just the right medicine for membranes, Adv. Funct. Mater. 28 (8) (2018), 1705327.
[28] T.H. Anderson, J. Yu, A. Estrada, M.U. Hammer, J.H. Waite, J.N. Israelachvili, The contribution of DOPA to substrate-peptide adhesion and internal cohesion of mussel-inspired synthetic peptide films, Adv. Funct. Mater. 20 (23) (2010) 4196–4205.
[29] L. Wang, H. He, X. Yang, Y. Zhang, S. Xiong, C. Wang, X. Yang, B. Chen, Q. Wang, Bimetallic ions regulated PEEK of bone implantation for antibacterial and osteogenic activities, Mater. Today Adv. 12 (2021), 100162.
[30] Z. Yang, Y. Xi, J. Bai, Z. Jiang, S. Wang, H. Zhang, W. Dai, C. Chen, Z. Gou, G. Yang, C. Gao, Covalent grafting of hyperbranched poly-L-lysine on Ti-based implants achieves dual functions of antibacteria and promoted osteointegration in vivo, Biomaterials 269 (2021), 120534.
[31] L. Tian, Z. Zhang, B. Tian, X. Zhang, N. Wang, Study on antibacterial properties and cytocompatibility of EPL coated 3D printed PCL/HA composite scaffolds, RSC Adv. 10 (8) (2020) 4805–4816.
[32] Y. Zhang, F. Wang, Q. Huang, A.B. Patil, J. Hu, L. Fan, Y. Yang, H. Duan, X. Dong, C. Lin, Layer-by-layer immobilizing of polydopamine-assisted epsilon-polylysine and gum Arabic on titanium: tailoring of antibacterial and osteogenic properties, Mater. Sci. Eng. C 110 (2020), 110690.
[33] I. Muhamed, E.P. Sproul, F.S. Ligler, A.C. Brown, Fibrin nanoparticles coupled with keratinocyte growth factor enhance the dermal wound-healing rate, ACS Appl. Mater. Interfaces 11 (4) (2019) 3771–3780.
[34] M. Bacakova, J. Pajorova, T. Sopuch, L. Bacakova, Fibrin-modified cellulose as a promising dressing for accelerated wound healing, Materials 11 (11) (2018) 2314.
[35] R. Ye, H. Xu, C. Wan, S. Peng, L. Wang, H. Xu, Z.P. Aguilar, Y. Xiong, Z. Zeng, H. Wei, Antibacterial activity and mechanism of action of epsilon-poly-L-lysine, Biochem. Biophys. Res. Commun. 439 (1) (2013) 148–153.
[36] K. Ushimaru, Y. Hamano, H. Katano, Antimicrobial activity of epsilon-Poly-l-lysine after forming a water-insoluble complex with an anionic surfactant, Biomacromolecules 18 (4) (2017) 1387–1392.
[37] H. Yu, L. Liu, X. Li, R. Zhou, S. Yan, C. Li, S. Luan, J. Yin, H. Shi, Fabrication of polylysine based antibacterial coating for catheters by facile electrostatic interaction, Chem. Eng. J. 360 (2019) 1030–1041.
[38] Y. Wang, F. Wang, H. Zhang, B. Yu, H. Cong, Y. Shen, Antibacterial material surfaces/interfaces for biomedical applications, Appl. Mater. Today 25 (2021), 101192.
[39] G. Decher, Fuzzy nanoassemblies: toward layered polymeric multicomposites, Science 277 (5330) (1997) 1232–1237.
[40] M.M. De Villiers, D.P. Otto, S.J. Strydom, Y.M. Lvov, Introduction to nanocoatings produced by layer-by-layer (LbL) self-assembly, Adv. Drug Deliv. Rev. 63 (9) (2011) 701–715.
[41] S.L. Bellis, Advantages of RGD peptides for directing cell association with biomaterials, Biomaterials 32 (18) (2011) 4205–4210.
[42] J. Pajorova, M. Bacakova, J. Musilkova, A. Broz, D. Hadraba, F. Lopot, L. Bacakova, Morphology of a fibrin nanocoating influences dermal fibroblast behavior, Int. J. Nanomed. 13 (2018) 3367–3380.
[43] M. Wasilewska, Z. Adamczyk, M. Ocwieja, D. Wojnar, P. Zeliszewska, Silver nanoparticle/fibrinogen bilayers - mechanism of formation and stability determined by in situ electrokinetic measurements, J. Colloid Interface Sci. 513 (2018) 170–179.
[44] L. Wang, Y. Wu, T. Hu, P.X. Ma, B. Guo, Aligned conductive core-shell biomimetic scaffolds based on nanofiber yarns/hydrogel for enhanced 3D neurite outgrowth alignment and elongation, Acta Biomater. 96 (2019) 175–187.
[45] J. Zhong, S. Chen, Y. Zhao, J. Yin, Y. Wang, H. Gong, X. Zhang, J. Wang, Y. Wu, W. Huang, Shape Optimization of Costal Cartilage Framework fabrication based on finite element analysis for reducing incidence of auricular reconstruction complications, Front. Bioeng. Biotechnol. 9 (2021), 766599.
[46] Y. Sakamoto, Y. Nakanishi, M. Chen, T. Kiuchi, K. Kishi, Self-portrait distortion by selfies: increased desire for aesthetic surgery among millennials? J. Plast. Reconstr. Aesthetic Surg. 74 (6) (2021) 1355–1401.
[47] I. Bruzauskaite, D. Bironaite, E. Bagdonas, E. Bernotiene, Scaffolds and cells for tissue regeneration: different scaffold pore sizes-different cell effects, Cytotechnology 68 (3) (2016) 355–369.
[48] Y. Wang, H.I. Chang, D.F. Wertheim, A.S. Jones, C. Jackson, A.G. Coombes, Characterisation of the macroporosity of polycaprolactone-based biocomposites and release kinetics for drug delivery, Biomaterials 28 (31) (2007) 4619–4627.
[49] H. Amani, H. Arzaghi, M. Bayandori, A.S. Dezfuli, H. Pazoki-Toroudi, A. Shafiee, L. Moradi, Controlling cell behavior through the design of biomaterial surfaces: a focus on surface modification techniques, Adv. Mater. Interfac. 6 (13) (2019), 1900572.
[50] M. Meemusaw, R. Magaraphan, Surface and bulk properties improvement of HDPE by a batch plasma treatment, J. Appl. Polym. Sci. 133 (7) (2016), 43011.
[51] L. Cai, J. Lu, V. Sheen, S. Wang, Optimal poly(L-lysine) grafting density in hydrogels for promoting neural progenitor cell functions, Biomacromolecules 13 (5) (2012) 1663–1674.
[52] D. Campoccia, L. Montanaro, C.R. Arciola, The significance of infection related to orthopedic devices and issues of antibiotic resistance, Biomaterials 27 (11) (2006) 2331–2339.
[53] L. Hobley, C. Harkins, C.E. MacPhee, N.R. Stanley-Wall, Giving structure to the biofilm matrix: an overview of individual strategies and emerging common themes, FEMS Microbiol. Rev. 39 (5) (2015) 649–669.
[54] M.L. Martin, S.A. Dassie, L.E. Valenti, C.E. Giacomelli, A simple surface biofunctionalization strategy to inhibit the biofilm formation by Staphylococcus aureus on solid substrates, Colloids Surf. B Biointerfaces 183 (2019), 110432.
[55] D. Zhang, Q. Chen, C. Shi, M. Chen, K. Ma, J. Wan, R. Liu, Dealing with the foreign-body response to implanted biomaterials: strategies and applications of new materials, Adv. Funct. Mater. 31 (6) (2020), 2007226.
[56] Y. Xi, J. Ge, M. Wang, M. Chen, W. Niu, W. Cheng, Y. Xue, C. Lin, B. Lei, Bioactive Anti-inflammatory, Antibacterial, Antioxidative silicon-based nanofibrous dressing enables cutaneous tumor photothermo-chemo therapy and infection-induced wound healing, ACS Nano 14 (3) (2020) 2904–2916.
[57] G. Zhou, H. Jiang, Z. Yin, Y. Liu, Q. Zhang, C. Zhang, B. Pan, J. Zhou, X. Zhou, H. Sun, D. Li, A. He, Z. Zhang, W. Zhang, W. Liu, Y. Cao, In vitro regeneration of patient-specific ear-shaped cartilage and its first clinical application for auricular reconstruction, EBioMedicine 28 (2018) 287–302.
[58] I.A. Otto, P.E. Capendale, J.P. Garcia, M. de Ruijter, R.F.M. van Doremalen, M. Castilho, T. Lawson, M.W. Grinstaff, C.C. Breugem, M. Kon, R. Levato, J. Malda, Biofabrication of a shape-stable auricular structure for the reconstruction of ear deformities, Mater. Today Bio. 9 (2021), 100094.
[59] A. Peramo, C.L. Marcelo, Bioengineering the skin-implant interface: the use of regenerative therapies in implanted devices, Ann. Biomed. Eng. 38 (6) (2010) 2013–2031.
[60] W. Hu, Z. Wang, Y. Zha, X. Gu, W. You, Y. Xiao, X. Wang, S. Zhang, J. Wang, High flexible and broad antibacterial nanodressing induces complete skin repair with angiogenic and follicle regeneration, Adv. Healthc. Mater. (2020), 2000035.
[61] A. Marrella, T.Y. Lee, D.H. Lee, S. Karuthedom, D. Syla, A. Chawla, A. Khademhosseini, H.L. Jang, Engineering vascularized and innervated bone biomaterials for improved skeletal tissue regeneration, Mater, Today Off. 21 (4) (2018) 362–376.